Research Article Vol. 12, No. 6 / 1 June 2021 / Biomedical Optics Express 3700

Biomedical Optics EXPRESS

Multicolor structured illumination microscopy and quantitative control of polychromatic light with a digital micromirror device

PETER T. BROWN,[1] RORY KRUITHOFF,[1] GREGORY J. SEEDORF,[2] AND DOUGLAS P. SHEPHERD[1,*]

[1] Department of Physics and Center for Biological Physics, Arizona State University, Tempe, AZ 85287, USA
[2] Department of Pediatrics and Pediatric Heart Lung Center, University of Colorado Anschutz Medical Campus, Aurora, CO 80045, USA
[*] douglas.shepherd@asu.edu

Abstract: Linear structured illumination microscopy (SIM) is a super-resolution microscopy technique that does not impose photophysics requirements on fluorescent samples. Multicolor SIM implementations typically rely on liquid crystal on silicon (LCoS) spatial light modulators (SLM's) for patterning the excitation light, but digital micromirror devices (DMD's) are a promising alternative, owing to their lower cost and higher speed. However, existing coherent DMD SIM implementations use only a single wavelength of light, limited by the lack of efficient approaches for solving the blazed grating effect for polychromatic light. We develop the requisite quantitative tools, including a closed form solution of the blaze and diffraction conditions, forward models of DMD diffraction and pattern projection, and a model of DMD aberrations. Based on these advances, we constructed a three-color DMD microscope, quantified the effect of aberrations from the DMD, developed a high-resolution optical transfer function measurement technique, and demonstrated SIM on fixed and live cells. This opens the door to applying DMD's in polychromatic applications previously restricted to LCoS SLM's.

© 2021 Optical Society of America under the terms of the OSA Open Access Publishing Agreement

1. Introduction

The development of wavefront control using spatial light modulators (SLM's) has enabled a variety of techniques relevant to the study of biological and atomic systems, including quantitative phase imaging [1,2], optical trapping [3–5], adaptive optics [6], production of arbitrary dynamic optical potentials, and quantum gas microscopy [7,8]. SLM's are highly reconfigurable, which allows experiments to be modular and take advantage of dynamic light patterns. They are also highly reproducible and offer microscopic control of wavefronts, which allows precise calibration of optical systems and enhances quantitative modeling of experiments. Due to this broad applicability, advancements in optical methodology for SLM's have had an immediate impact for many fields of quantitative imaging.

The study of biological regulation at the molecular level is one field that has greatly benefited from advancements in optical methodologies. For example, the development of super-resolution (SR) microscopy has allowed optical study of biological systems below the diffraction limit, on the 1 nm–200 nm scale. Despite the promise of sub-diffraction studies of molecular interactions, SR techniques have yielded limited insight into the temporal dynamics of molecular regulation within living cells and larger systems. One barrier is that all SR methods impose a trade-off between imaging speed, resolution, sample preparation, and fluorophore photophysics. For example, single molecule localization microscopy (SMLM) trades temporal resolution for spatial resolution, requiring fixed samples and repeated imaging of fluorophores with specific photophysics [9,10]. Computational methods that infer SR information from fluctuating signals relax the above requirements, but require acquisition, processing, and merging of many imaging

#422703 https://doi.org/10.1364/BOE.422703
Journal © 2021 Received 23 Feb 2021; revised 14 May 2021; accepted 17 May 2021; published 1 Jun 2021

Biomedical Optics EXPRESS

frames [11,12]. Stimulated emission depletion (STED) requires a high intensity depletion beam, careful alignment of the depletion and excitation beams, specific fluorophores, and raster scans to build an image [13,14]. MINFLUX and MINSTED lower the total intensity incident on the sample as compared to STED, but still require raster scanning [15,16]. Methods such as MoNaLISA parallelize the application of depletion and saturation to imaging, but require precise 3D pattern projection and specific fluorophore photophysics [17,18]. In contrast to the above methods, linear structured illumination microscopy (SIM) does not impose specific sample requirements. The trade-off for this flexibility is a modest increase in high frequency content for linear SIM, requirement for high-quality control of the excitation light, and potentially slow imaging rates. New quantitative approaches that both simplify the construction and increase the speed of multicolor SIM would provide researchers with a flexible platform to measure temporal dynamics below the classical diffraction limit using standard sample preparations.

Here, we briefly outline the working principles, current state-of-the-art, and limitations of existing SIM instruments. SIM obtains SR information by projecting a structured illumination pattern on the sample and relying on the moiré effect to down-mix high-frequency sample information below the system band limit. It was first proposed as an SR technique in [19,20], but a similar technique was previously exploited for optical sectioning (OS) [21,22]. Early implementations achieved SR in the lateral direction only (2D-SIM) [23,24], while later approaches also enhanced the axial resolution (3D-SIM) [25–28]. Initial experiments utilized diffraction gratings to produce SIM patterns and required both separate paths for multiple colors and physical translation and rotation, which severely limited their speed [27]. Various advances in LCoS SLM's, sCMOS cameras, and GPU's have enabled much faster 2D [29–34] and 3D SIM [35], and multicolor SIM with a single optical path [36]. Recent experiments have exploited structured light and statistical techniques to increase the precision of localization microscopy [37–41]. The quality of the obtained SIM reconstructions is highly dependent on the modulation depth of the projected patterns and any other deviations from the ideal optical transfer function used to weight the different frequency components. As the complexity of the desired result increases from obtaining optical sectioning to multicolor 3D-SIM, so does the required fidelity in the final projected patterns. This has led to wide spread adoption of LCoS SLM's as a diffractive optic for SIM, despite their drawbacks which include cost, complex experimental timing, and relatively slow speed.

Digital micromirror devices (DMD's) are a promising alternative to LCoS SLM's for a variety of wavefront shaping tasks. DMD's offer several advantages, including a factor of 2–10 lower cost, less experimental timing complexity, and a factor of 5–10 imaging rate increase [42–44]. DMD's can reach frame rates of up to 30 kHz, exceeding the rates achievable in ferroelectric and nematic LCoS SLM's by factors of ~5 and ~10 respectively. Unlike ferroelectric SLM's, DMD's do not require the pattern to be inverted every ~100 ms. Finally, the amplitude-only modulation characteristic of the DMD allows fast, well-defined diversion of the illumination beam from the sample, making an additional fast shutter unnecessary. However, DMD use is currently limited by a computationally expensive forward model [43] to evaluate the blazed grating effect, which enhances the diffraction efficiency into a single order but also imposes severe restrictions on multicolor operation. To date, DMD based approaches for sinusoidal pattern SIM, referred to as SIM from here onward, have used incoherent projection [45] or one coherent wavelength [37,43,44]. Incoherent projection SIM at best provides an order of magnitude lower signal-to-noise ratio, leading to inferior experimental resolution, despite previously reported erroneous resolution measurements [45,46] (Supplemental Note 1, Supplement 1).

In this work, we overcome these difficulties to realize a flexible, three-color DMD-SIM using coherent light. We achieve this by creating analytic forward models of both diffraction from the DMD and SIM pattern projection which limit computation time by identifying the discrete set of diffracted frequencies generated by a given pattern. Next, we harness these models to

Biomedical Optics EXPRESS

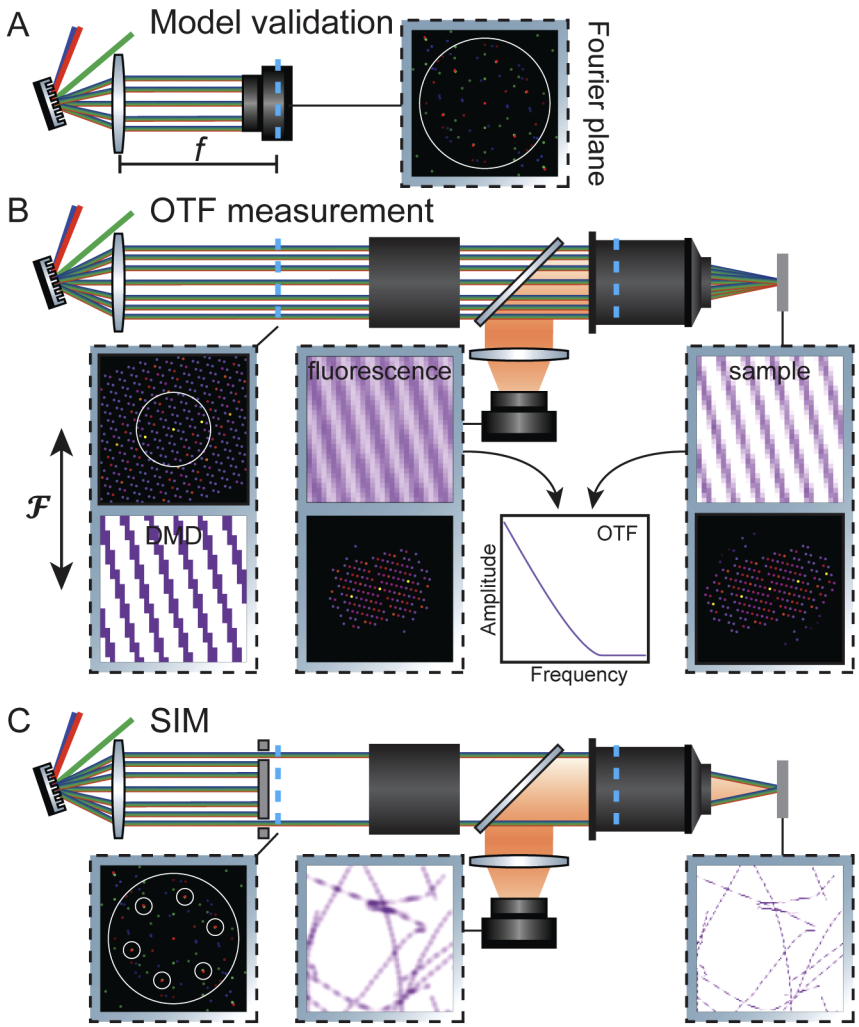

Fig. 1. Experiment schematic. **A**. Optical system for DMD and pattern forward model verification. The Fourier mask and polarization optics are removed and the camera is placed in the back focal plane of the first lens (dashed blue line). **B**. Optical system for OTF mapping. The Fourier mask and polarization optics are removed from the system, so all diffraction orders within a certain angular spread pass through the pupil (left inset). Dashed blue lines indicate the objective back focal plane and its conjugates. The diffraction orders are imaged onto a flat sample (right inset) by additional optics (black box). Fluorescence from the sample is imaged by the camera (center left inset). Predictions for the sample plane illumination based on the forward models is compared with the measured intensity to extract the OTF (center right inset). In each inset, the top image shows the light intensity, while the bottom shows its Fourier transform. For the real space images low (high) intensity is shown in white (purple), while for the Fourier space images low (high) intensity is shown in black (colors increasing from purple to yellow). **C**. Optical system for SIM imaging. Three wavelengths diffract from the DMD. A mask in the Fourier plane passes the six SIM diffraction orders. The diffraction orders are shown for all nine SIM patterns (left inset) and 465 nm (blue), 532 nm (green), and 635 nm (red) and the shape of the mask is illustrated (white circles). The SIM patterns are projected on the sample plane (right inset) and imaged on the camera (middle inset).

Biomedical Optics EXPRESS

design an experimental optical configuration that satisfies the unique requirements the DMD imposes when used as a polychromatic diffractive optic. Finally, we employ this apparatus in three applications, illustrated in Fig. 1(A), B, and C respectively: (1) we validate these forward models by performing a detailed comparison between the positions and intensities of diffraction peaks generated by hundreds of SIM patterns, (2) we develop a calibration routine to directly map the optical transfer function (OTF) of the system without the need to estimate it from sub-diffraction limited fluorescent microspheres, and (3) we realize three wavelength, 2D linear SIM of calibration samples, fixed cells, and live cells. These applications illustrate the potential of this framework to enhance rational and quantitative design of DMD based instruments.

2. Methods

Leveraging the advantages of the DMD as a polychromatic diffractive optic requires a tractable forward model of diffraction from the displayed DMD patterns. To this end, we developed an analytic solution of the combined blaze and diffraction condition for arbitrary wavelengths and incidence angles (Supplemental Note 2, Supplement 1) and derived analytical forward models of DMD diffraction and pattern projection which we validated experimentally (Supplemental Notes 3-4, Supplement 1). We also applied these models to assess the effects of DMD aberrations on pattern formation. This provides an alternative framework to a previously published numerical simulation approach [43].

2.1. DMD diffraction forward model

To develop the DMD forward model, we calculate the diffracted light profile for an incident plane wave in the Fraunhofer approximation by considering the phase shift introduced by each point on the micromirror surfaces [43,47–49]. We adopt the same coordinate system as [43], where the DMD normal is along the $-\hat{\mathbf{z}}$ direction, the micromirrors are organized in a regular grid aligned with the $\hat{\mathbf{x}}$ and $\hat{\mathbf{y}}$ directions, and the micromirrors swivel about an axis along the $(\hat{\mathbf{x}}+\hat{\mathbf{y}})/\sqrt{2}$ direction. For a plane wave of wave vector $k = 2\pi/\lambda$ incident along direction $\hat{\mathbf{a}}$, the diffracted electric field in direction $\hat{\mathbf{b}}$ is

$$\begin{aligned} E(\hat{\mathbf{b}}) =& E_o \sum_{m_x,m_y} \exp\left(-ik(dm_x, dm_y, z(m_x,m_y)) \cdot (\hat{\mathbf{b}}-\hat{\mathbf{a}})\right) \\ &\times w^2 \operatorname{sinc}\left(\frac{kw}{2}A_+(\gamma_{m_x,m_y})\right) \operatorname{sinc}\left(\frac{kw}{2}A_-(\gamma_{m_x,m_y})\right) \end{aligned} \tag{1}$$

$$A_\pm(\gamma, \hat{\mathbf{a}}-\hat{\mathbf{b}}) = \frac{1\pm\cos\gamma}{2}(a_x-b_x) + \frac{1\mp\cos\gamma}{2}(a_y-b_y) \mp \frac{\sin\gamma}{\sqrt{2}}(a_z-b_z), \tag{2}$$

where γ_{m_x,m_y} is the angle the mirror at position (m_x, m_y) makes with grating normal, $z(m_x, m_y)$ is the surface height of the DMD, w is the mirror width, and d is the spacing between adjacent mirrors. At each mirror γ takes one of two values: either $+12°$ ("on") or $-12°$ ("off"). Here the sinc envelope expresses the effect of rays interfering from the same micromirror, and the sum represents rays interfering from different micromirrors. The surface height $z(m_x, m_y)$ reflects the possible presence of aberrations due to DMD chip manufacturing imperfections.

To incorporate DMD diffraction into the overall optical system response, we recast the effect of the DMD as an effective pupil function. To do this we define the pattern function, $P(m_x, m_y)$ where we take $P = 0$ ($P = 1$) at "off" ("on") mirrors. We recognize that in the absence of aberrations (i.e. $z(m_x, m_y) = 0$) Eq. (1) gives the discrete Fourier transform (DFT) of the pattern

Biomedical Optics EXPRESS

function, $\tilde{P}$, therefore the diffracted electric field becomes

$$E(\mathbf{f}) = \tilde{P}(\mathbf{f})H_{\mathrm{DMD}}(\mathbf{f}) \tag{3}$$

$$H_{\mathrm{DMD}}(\mathbf{f}) = w^2 \mathrm{sinc}\left[A_+\left(\gamma, \hat{\mathbf{a}} - \hat{\mathbf{b}}(\mathbf{f})\right)\right] \mathrm{sinc}\left[A_-\left(\gamma, \hat{\mathbf{a}} - \hat{\mathbf{b}}(\mathbf{f})\right)\right] \tag{4}$$

where $\mathbf{f}$ is the spatial frequency of the DMD image and $\hat{\mathbf{b}}(\mathbf{f})$ is the output unit vector diffracted by the pattern component at $\mathbf{f}$. We ignore the "off" state mirrors in this equation, as we are only considering frequencies near a single solution of the diffraction condition, and the sinc envelopes for the "on" and "off" state mirrors are typically well separated.

The complete information about the pattern is contained in a discrete set of output angles (frequencies) given by the DFT frequencies

$$\frac{b_{x,y}(\mathbf{f}) - a_{x,y}}{\lambda} = \frac{1}{d}\left(\frac{n_x}{N_x}, \frac{n_y}{N_y}\right), \; n_x, n_y \in \mathbb{Z}. \tag{5}$$

When n_x (n_y) is a multiple of N_x (N_y) Eq. (5) is the diffraction condition for the underlying grating. Other frequencies are generated by diffraction from the DMD pattern. For a finite pixel grid, intermediate frequencies can be calculated from the DFT using an analog of the Whittaker-Shannon interpolation formula.

Equations (3)–(5) constitute a complete forward model of DMD diffraction. The expressions obtained here remove the need to numerically evaluate integrals or perform other expensive numerical simulations to determine DMD diffraction. It is only necessary to calculate a discrete Fourier transform, solve for output angles, and evaluate the sinc factor.

2.2. Multicolor DMD diffraction

We now apply our forward model to evaluate the constraints it places on multicolor operation. We first specialize to the plane in which the micromirrors swivel, i.e. the $(x - y)\, z$ plane, which simplifies the analysis because light incident in this plane has its primary diffraction orders in the same plane. For light incoming and outgoing in this plane, the blaze and diffraction conditions reduce to [47],

$$\theta^a - \theta^b = 2\gamma \tag{6}$$

$$\sin\theta^a - \sin\theta^b = \sqrt{2}\frac{\lambda_i}{d} n_i, \tag{7}$$

where $\theta^{a,b}$ are the angles between $\hat{\mathbf{a}}$ or $\hat{\mathbf{b}}$ and the DMD normal in the $(x - y)\, z$ plane and i indexes the different wavelengths. The blaze condition (Eq. (6)) gives the angle where the law of reflection is satisfied for light incident on a single micromirror [47]. For N wavelengths, this is a system of $N + 1$ equations with two angles and N diffraction orders as free parameters. In Supplemental Note 2 in Supplement 1 we show the blaze and diffraction conditions can be solved analytically for arbitrary input angles.

To realize multicolor operation we must solve this system for $N>1$, which we achieve by first solving the blaze and diffraction conditions for λ_1, and then attempting to satisfy $\frac{\lambda_i}{\lambda_j} = \frac{n_j}{n_i}$. This ratio condition can be solved by finding rational approximations to each of these, $\frac{\lambda_i}{\lambda_1} = \frac{p_i}{q_i}$. Then an approximate solution is obtained from $n_1 = \mathrm{lcm}(p_1, \ldots, p_N)$ and $n_i = \frac{q_i n_1}{p_i}$. Any deviation between the rational approximation and the wavelength ratio must be accounted for by changing the input angle of the incident light, which entails slight violation of the blaze condition.

Additional colors can also be injected using the DMD mirror "off" state. Supposing we have already fixed the input and output angle for several colors using the "on" state mirrors, additional

Biomedical Optics EXPRESS

wavelengths must satisfy

$$\sin(\theta^a - 4\gamma) - \sin(\theta^a - 2\gamma) = \sqrt{2}\frac{\lambda}{d}n. \tag{8}$$

We provide a full solution for two color operation using one "on" and one "off" diffraction order in Supplemental Note 2 (Supplement 1).

For our DMD parameters, $d = 7.56$ µm and $\gamma = 12°$, two color operation can be achieved using $\lambda_1 = 465$ nm, $\lambda_2 = 635$ nm, by approximating $\lambda_2/\lambda_1 \sim 4/3$ which implies $n_1 = 4, n_2 = 3$, with $\theta^a = 45.20°$ and $\theta^b \sim 21.20°$. Adding a third wavelength, $\lambda_3 = 532$ nm, using this approach is challenging because the smallest rational approximation with less than 10 % error is $\lambda_3/\lambda_1 \sim 8/7$, implying $n_1 = 8, n_2 = 7, n_3 = 6$. However, the maximum diffraction orders allowed by Eqs. (6) and (7) are $n_{\max} = 4, 3, 3$ respectively. Instead, we achieve three color operation by injecting 532 nm light using $\theta^a = -2.09°$ and the −4th order from the "off" mirrors. Overlapping the 532 nm diffraction with the other colors requires a deviation of ~0.7° from the blaze condition. Perfect alignment of the −4th order occurs near 550 nm.

Deviations from the blaze condition degrade the SIM modulation contrast. To quantify this degradation, let η be the imbalance between the two components of the diffracted electric field that interfere to produce the SIM pattern. The pattern modulation contrast is the ratio of amplitudes of the high frequency and DC components of the intensity pattern,

$$m = \frac{2\eta}{1 + \eta^2}. \tag{9}$$

The contrast depends on the angle of the SIM pattern, ranging from a minimum along the $\theta_x = -\theta_y$ direction to a maximum along the $\theta_x = \theta_y$ direction. We summarize the worst case contrast for our parameters in Table 1 and Fig. 2, where we find high contrast is expected despite the modest violation of the blaze condition at 532 nm and 635 nm. The ultimate SIM performance is determined by the modulation depth, which is sensitive to the modulation contrast, the available laser power, and the brightness of the sample.

Table 1. Comparison of design input and output angles and modulation contrast degradation in SIM patterns due to violation of the blaze condition versus wavelength for the mirror patterns shown in Fig. 2.

wavelength	θ^a	θ^b	diffraction order	blaze deviation	η^2	m
465 nm	45.20°	21.20°	(4, -4)	0°	1	1
532 nm	−2.09°	21.20°	(-4, 4)	0.71°	0.718	0.986
635 nm	45.89°	21.20°	(3, -3)	0.69°	0.850	0.997

2.3. DMD SIM forward model

To quantitatively characterize SIM pattern formation in our system, we apply the DMD forward model to a set of mirror patterns commonly employed to generate SIM sinusoidal illumination profiles. SIM patterns are designed to be periodic to maximize diffraction into a single spatial frequency component. We define SIM patterns on a small subset of DMD mirrors, the unit cell, which is tiled across the DMD by a pair of lattice vectors, $\mathbf{r}_1$ and $\mathbf{r}_2$, which have integer components. This produces a periodic pattern in the sense that mirrors separated by $n\mathbf{r}_1 + m\mathbf{r}_2$ for any $n, m \in \mathbb{Z}$ will be in the same state.

The lattice structure implies all frequency components of the SIM pattern are multiples of the reciprocal lattice vectors, $\mathbf{k}_{1,2}$, defined by the property $\mathbf{r}_i \cdot \mathbf{k}_j = \delta_{ij}$ [50]. This constrains the frequencies of the diffracted electric field to the set $\mathbf{f} = n_1\mathbf{k}_1 + n_2\mathbf{k}_2$. Furthermore, the Fourier

Biomedical Optics EXPRESS

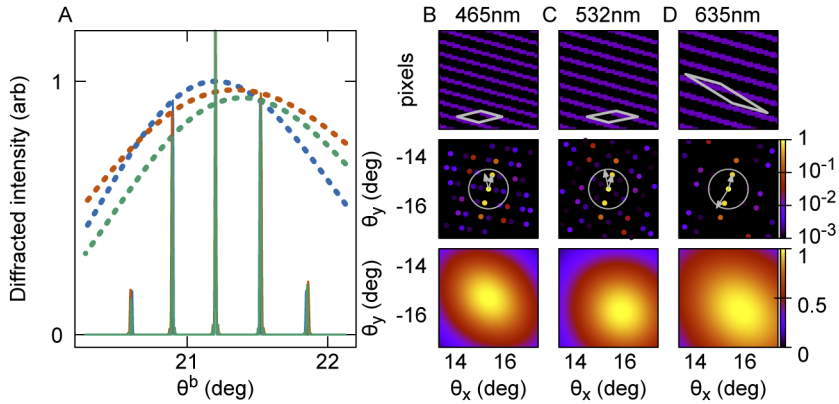

Fig. 2. DMD diffraction forward model. **A**. Diffracted intensity for $\lambda = 465$ nm (blue), 532 nm (green), and 635 nm (red) along the SIM order diffraction direction. For these input angles, 465 nm satisfies the Blaze condition while 532 nm and 635 nm show some deviation, visible in the shift of the envelope center and the asymmetry in the diffraction peaks. **B**. DMD mirror pattern showing "on" mirrors (purple), "off" mirrors (black), and one unit cell (gray outline) for the experimental mirror patterns given in table S2. Diffracted intensity from the DMD using 465 nm light shown on a log scale. The maximum acceptance angle (gray circle) and reciprocal vectors (gray arrows) are shown (center panel). The envelope function illustrating where the blaze condition is satisfied, shown with a linear scale. **C**. 532 nm patterns and DMD diffraction effects. **D**. 635 nm patterns and DMD diffraction effects.

components can be calculated from the unit cell U, which is typically much smaller than the full DMD,

$$\tilde{P}(s,t) = \sum_{(i,j)\in U} P(i,j) \exp\left[-2\pi i(i,j)\cdot(s\mathbf{k}_1 + t\mathbf{k}_2)\right]. \tag{10}$$

This expression is correct up to a boundary term when the unit cell does not perfectly tile the DMD.

To generate appropriate SIM patterns for the experiment we construct $\mathbf{r}_{1,2}$ such that $\mathbf{k}_2$ matches a desired period P and angle θ (see Supplemental Note 6, Supplement 1). We also require that the pattern can be translated to change its phase, which is achieved by setting $\mathbf{r}_2 = (n,m)n_p$ where n_p is the number of desired SIM phases [31,32,35,36]. Next, we construct one unit cell of our pattern by generating a smaller cell U_p from the vectors $\mathbf{r}_1$ and $\mathbf{r}_2/n_p$. By construction U_p is contained in U. Setting all pixels in U_p to "on" and all other pixels in U to "off" creates the desired pattern, which has Fourier components

$$\tilde{P}(s,t) = \sum_{(i,j)\in U_p} \exp\left[-2\pi i(i,j)\cdot(s\mathbf{k}_1 + t\mathbf{k}_2)\right]. \tag{11}$$

The strongest Fourier component of this pattern occurs at $\mathbf{k}_2$, which defines the SIM frequency. However the pattern also has Fourier weight at other reciprocal lattice vectors due to its binary and pixelated nature. These additional Fourier components introduce unwanted structure in the SIM patterns, and are blocked in the experiment by inserting a mask in the Fourier plane.

Although these Fourier components are unwanted in SIM operation, our ability to precisely predict their amplitude and frequency can be used to extract information about either our optical system or a sample of interest. These predictions are highly accurate (Supplemental Note 3 in Supplement 1), and hence can be used to map out the frequency response of our imaging system (Fig. 1) . In the future this information could also be harnessed to enhance SIM reconstruction.

Biomedical Optics EXPRESS

The unit cell can also be applied to simplify the analysis of DMD aberrations for SIM patterns. If we assume that the DMD height varies slowly on the scale of one unit cell, we can take $z(n_1\mathbf{r}_1 + n_2\mathbf{r}_2)$ to be the average height at unit cell at position $n_1\mathbf{r}_1 + n_2\mathbf{r}_2$. If the DMD flatness varies more quickly then discrete diffraction orders will be difficult to resolve, which is not the case experimentally. Using this simplification, Eq. (1) becomes

$$E(\hat{\mathbf{b}}) = \left[\sum_{(m_x,m_y)\in U} P(m_x, m_y) \exp\left(-ikd(m_x, m_y, 0)\cdot(\hat{\mathbf{b}} - \hat{\mathbf{a}})\right)\right] \times \left[\sum_{n_1,n_2} \exp\left(-ik\left[n_1\mathbf{r}_1 + n_2\mathbf{r}_2 + z(n_1\mathbf{r}_1 + n_2\mathbf{r}_2)\hat{\mathbf{z}}\right]\cdot(\hat{\mathbf{b}} - \hat{\mathbf{a}})\right)\right] H_{\mathrm{DMD}}, \tag{12}$$

which is more efficient to compute than Eq. (1). Here the first bracketed term is equivalent to Eq. (10), while the second reflects incomplete interference between diffraction from different unit cells.

We demonstrate the effect of this model assuming an astigmatic type aberration of the DMD of roughly 3λ, similar to what was observed in [7]. The results are shown in Fig. 3. The primary

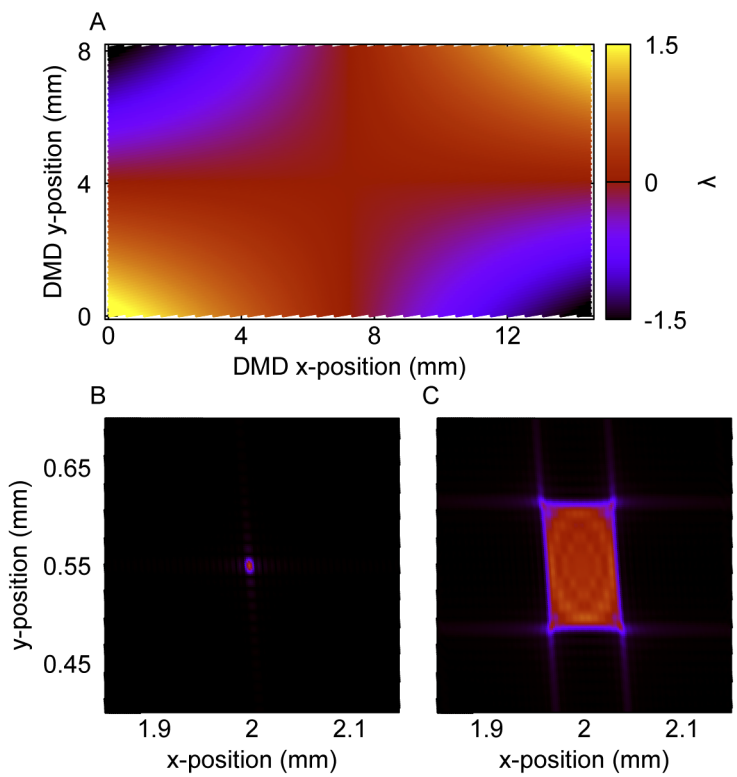

Fig. 3. DMD aberration simulation. DMD aberration simulation for a SIM pattern with $\mathbf{r}_1 = (-3, 11)$ and $\mathbf{r}_2 = (3, 12)$. **A**. DMD aberration profile in units of wavelengths. **B**. One diffraction order in the Fourier plane, without aberrations. The standard deviations along the x and y directions are ~8 µm and 11 µm respectively. The size of the order is limited by the finite size of the DMD, and the shape is asymmetric because the DMD is rectangular. **C**. One diffraction order in the Fourier plane with aberrations. The standard deviations along the x and y directions are ~22 µm and 38 µm, approximately three times larger than in the unaberrated simulation.

Biomedical Optics EXPRESS

effect of these aberrations is to broaden the SIM diffraction orders in the Fourier plane. This occurs because the narrow diffraction orders are created by interference from the diffraction of many unit cells, but phase errors result in incomplete interference between these cells. This does not cause a problem for our experiment as long as the size of the diffraction orders is smaller than the holes in the Fourier mask. As shown in the figure, this level of aberration results in broadening on the order of 100 µm, significantly less than the 1 mm diameter of the Fourier mask holes used in the experiment.

To assess the aberrations present in our experiment, we measured the DMD flatness in our system using the technique of [7]. We find it is $\sim \lambda/2$ at 780 nm (Supplemental Note 5 in Supplement 1).

3. Results

We utilized the theoretical approach described above to design a DMD microscope for three-color coherent light operation at 465 nm or 473 nm, 532 nm, and 635 nm, and demonstrated our instrument's capabilities with three types of experiments. First, we validated the predictions of the DMD and SIM pattern forward models (Fig. 1(A),(B) and Supplemental Note 3 in Supplement 1). Then, we developed and realized a novel technique to measure the system optical transfer function. Finally, we validated our instrument's 2D SIM capabilities by imaging a variety of samples. These samples include an Argo-SIM calibration sample, which shows our instrument produces SR information in all spatial directions and achieves resolution near the theoretical limit, and fixed and live cells, which demonstrate two- and three-color imaging with SR enhancement in biological systems. In addition to the various advantages of our approach discussed before, our instrument has a large field of view, 100 µm×90 µm, which is at least four times as large as typical DMD SIM [43,44] and LCoS SLM instruments [34,51]. Further details regarding the instrument design and sample preparation are provided in Supplemental Notes 7, 8, 9, and 10 in Supplement 1.

To support our instrument and disseminate our quantitative modeling tools, we created a Python-based software suite for computing forward models of DMD diffraction and pattern projection, DMD pattern design, OTF measurement analysis, simulation of SIM imaging given a ground truth structure, and 2D SIM reconstruction. Our SIM reconstruction algorithm is based on published work [52], with enhancements based on the ability to precisely calibrate fringe projection and direct measurement of the OTF (Supplemental Note 11, Supplement 1). We compared reconstruction results with FairSIM (Supplemental Note 12, Supplement 1) and explored their behavior versus signal-to-noise ratio (SNR) under a variety of conditions through simulation (Supplemental Note 13, Supplement 1). The software suite is available on GitHub (Code 1 [53]).

3.1. Optical transfer function determination

As a first demonstration of the advantages of our DMD and SIM pattern forward models for quantitative imaging, we apply them to directly measure the optical transfer function by projecting a sequence of SIM patterns, including all diffraction orders, on a fluorescent sample and comparing the strength of different Fourier components with the model predictions. Such an approach may also be useful for higher resolution pupil phase retrieval schemes [54].

To map the optical transfer function, we project a series of SIM patterns with different frequencies and angles on a sample slide containing a thin layer of dye and observe the fluorescence at the camera. To avoid additional complications, we remove all polarization optics along the DMD path. For each pattern, we extract the amplitudes of the Fourier peaks at many reciprocal lattice vectors. We normalize the peak heights by the DC pattern component to correct for laser intensity drift. Finally, we compare the result to the Fourier components of the intensity pattern predicted by our forward model. The ratio of the measured and predicted peak value

Biomedical Optics EXPRESS

gives the optical transfer function of the imaging system. The results of this measurement are shown in Fig. 4.

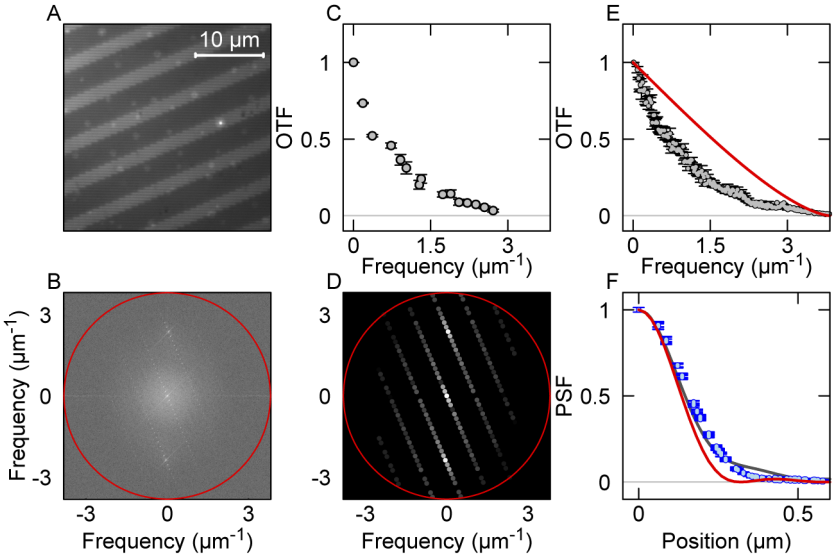

Fig. 4. Experimental optical transfer function determination. **A**. Image of Alexa Fluor 647 dye slide excited with 465 nm light and a DMD pattern with lattice vectors $\mathbf{r}_1 = (-107, -106)$ and $\mathbf{r}_2 = (111, 117)$. **B**. Power spectrum of image from A. illustrating the discrete set of pattern diffraction frequencies. The red line denotes the maximum frequency passed by the imaging system. **C**. Peak heights obtained from the Fourier transform of A. divided by the expected intensity components of the DMD pattern. Only peaks that are expected to be larger than 1 % of the DC value are shown. These provide an experimental estimate of the optical transfer function (gray points). Error bars are estimated from the noise power beyond the band cutoff. **D**. Theoretical power spectrum of the intensity pattern. The set of discrete frequency components predicted by the forward model matches that seen in the experiment. **E**. Experimental OTF (gray) determined with ~3800 peaks from 360 patterns as in C. These points are binned and the error bars represent the standard error of the mean. The red line is the theoretical optical transfer function for a circular aperture and NA = 1.3. **F**. Point spread functions corresponding to the OTF's shown in E., including the ideal PSF for a circular aperture (red), the PSF obtained from the OTF (gray), and the PSF obtained from imaging diffraction limited beads (blue).

The optical transfer function can be estimated from

$$H(\mathbf{f}_i) = \frac{I(\mathbf{f}_i)}{m(\mathbf{f}_i)e^{i\phi(\mathbf{f}_i)}}, \tag{13}$$

where I is the Fourier transform of the camera image, H is the optical transfer function, $\mathbf{f}_i$ are the allowed Fourier components of the DMD pattern, and the m and ϕ are the amplitude and phase of intensity pattern generated by the DMD (Supplemental Note 14, Supplement 1).

The experimental OTF rolls off more sharply than the ideal (Fig. 4(E)), which is expected for real optical systems. The point spread function obtained from the OTF agrees well with that obtained from diffraction limited beads (Fig. 4(F)). We use this experimental OTF in the reconstruction of our SIM data, which is expected to lead to more accurate reconstructions (Supplemental Note 13, Supplement 1).

This approach can also be applied in real samples if additional corrections for sample structure are included. Incorporating this quantitative OTF measurement technique with adaptive optics

Biomedical Optics EXPRESS

would allow sensorless real-time aberration correction similar to what was achieved in [55], but incorporating additional information from our quantitative model.

While this approach is of general use, knowledge of the OTF is particularly important in SIM because the reconstruction algorithm is highly sensitive to the optical transfer function, which is typically inferred from the point-spread function with low resolution because PSF's of Nyquist sampled imaging systems have support on only a few pixels.

3.2. Estimating SIM resolution from variably spaced line pairs

We assessed the experimental SIM resolution by measuring the Argo-SIM test slide (Fig. 5). This slide includes test patterns consisting of variably spaced line pairs, ranging from 390 nm to 0 nm in steps of 30 nm. There are four of these patterns in different orientations (0°, 45°, 90°, 135°), allowing determination of the SIM resolution in all directions. We only assessed performance in the 465 nm channel because the other channels do not efficiently excite fluorescence in the sample.

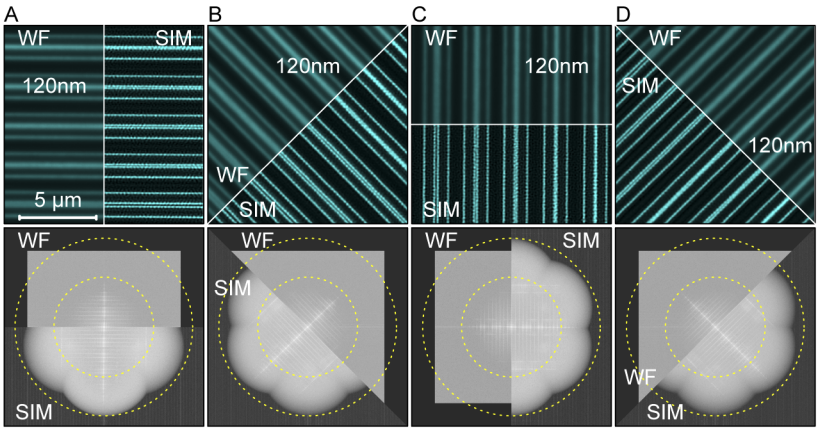

Fig. 5. Experimental characterization of SIM resolution. A. Widefield and SIM images of an Argo-SIM test pattern of closely spaced line pairs (each pair flanked by two additional lines) using 465 nm excitation light (top). This image illustrates line pairs with spacings of 210 nm–90 nm. Widefield and SIM power spectra (bottom). The smaller yellow circle illustrates the maximum frequency where the ideal optical transfer function has support for NA = 1.3 and emission wavelength 520 nm. The largest yellow circle represents the maximum frequency where the SIM reconstruction has support, which is about 1.78 times that of the widefield. This is <2 because the SIM pattern frequency does not saturate the diffraction limit. **B**., **C**., **D**. Images as in A. for Argo-SIM patterns in a different orientations. For all orientations except C., the line pair separated by 120 nm can be resolved in the SIM images. The orientation in C. falls along the seam between two SIM angles and thus has lower resolution, resolving only the 150 nm line pair. Images are displayed in analog-to-digital units (ADU).

The smallest line pair we resolved is separated by 120 nm (10th pair, Fig. 5). This should be compared with the minimum line spacing resolved by the widefield image, which is the 270 nm spaced pair (5th). However, the ability to resolve closely spaced objects is affected by contrast as well as resolution. To provide a quantitative and model-free characterization of SIM resolution, we assess the images using decorrelation analysis [56], which is available as an ImageJ plugin. Decorrelation analysis, which infers the resolution based on phase correlations in Fourier transform of the image, is expected to provide an accurate resolution estimate for sCMOS data, while Fourier Ring Correlation (FRC) is not [57–59]. For a conservative estimate of resolution

Biomedical Optics EXPRESS

enhancement, we report the relative resolution enhancement between the Wiener filtered widefield and SIM images. We propose that comparing Wiener filtered widefield and SIM is a more realistic measure of the information increase in the final SIM image. For the four images considered here the mean resolution enhancement is 1.54, and the maximum resolution enhancement is 1.58, corresponding to a resolution of ~130 nm. For an alternative test of instrument performance, we compared the size of diffraction limited fluorophores (see Supplemental Note 15.1, Supplement 1), and found an enhancement of 1.71.

The experimental resolution should be compared with the upper theoretical bound on SIM resolution set by the SIM pattern spacing, which is

$$f_{\max} = \frac{2\mathrm{NA}}{\lambda_{\mathrm{emission}}} + f_{\mathrm{SIM}} \leq \frac{2\mathrm{NA}}{\lambda_{\mathrm{emission}}} + \frac{2\mathrm{NA}}{\lambda_{\mathrm{excitation}}}, \tag{14}$$

neglecting situations where the excitation and emission NA differ, such as in TIRF SIM. The maximum resolution for $\lambda = 520$ nm, NA = 1.3, and SIM pattern period 250 nm–260 nm is ~110 nm, or a factor of ~1.78 enhancement over widefield. The maximum possible resolution enhancement is reduced from 2 to ~1.78 because we use a SIM pattern frequency that is 71 % of the maximum value allowed for our objective NA. The exact enhancement factor will depend on the Stokes shift for a given fluorophore. This choice of SIM pattern frequency is advantageous for reliable determination of the SIM pattern in realistic samples, where aberrations tend to obscure a higher pattern frequency.

Experimentally, the resolution is the maximum frequency where the image is not noise dominated (i.e. SNR $\gtrsim 1$). In low to moderate brightness samples, this may be significantly less than the theoretical resolution because the highest frequency SR information falls at the edge of the OTF, and the intensity must exceed the noise to be detectable. This is the case for many biological samples, and hence the resolution is sensitive to available laser power, fluorophore brightness, sample aberrations, and SIM pattern modulation contrast. We further explored the role of signal-to-noise ratio and the use of our calibrated OTF via simulations (Supplemental Note 13, Supplement 1). Although common practice, we do not apply post processing after SIM reconstruction (such as additional deconvolution or notch filtering) to enhance the reported SIM resolution.

3.3. Two-wavelength imaging of fixed cells

As an initial test of multicolor imaging using both "on" and "off" states of the DMD, we performed two wavelength SIM using the 473 nm and 532 nm channels to image actin filaments and mitochondria labeled with Alexa Fluor 488 and MitoTracker Red CMXRos in fixed bovine pulmonary artery endothelial (BPAE) cells. The SIM images substantially narrow the apparent width of the actin filaments (Fig. 6), in many cases making two filaments visible that were not distinguishable in the widefield image. The mitochondria similarly reveal cristae which cannot be distinguished in the widefield, but are visible in the SIM. Applying decorrelation analysis to the Wiener filtered widefield and SIM images, we find SIM leads to resolution enhancements by factors of ~1.5 and ~1.65 in the 473 nm and 532 nm channels respectively. We verified our reconstruction results using FairSIM (Supplemental Figure S6, Supplement 1) and further explored the role of SNR in filamentous networks via simulation (Supplemental Note 13, Supplement 1).

3.4. Three-wavelength imaging of live adenocarcinoma epithelial cells

We demonstrated time-resolved three-color SIM of live human adenocarcinoma cells by imaging mitochondria, actin, and lysosomes labeled with MitoTracker green, CellMask orange, and LysoTracker deep red. We imaged cell dynamics over a period of 15 min with a field of view of 100 µm×90 µm, taking images at 1 min intervals (see Visualization 1). We chose an exposure time

Biomedical Optics EXPRESS

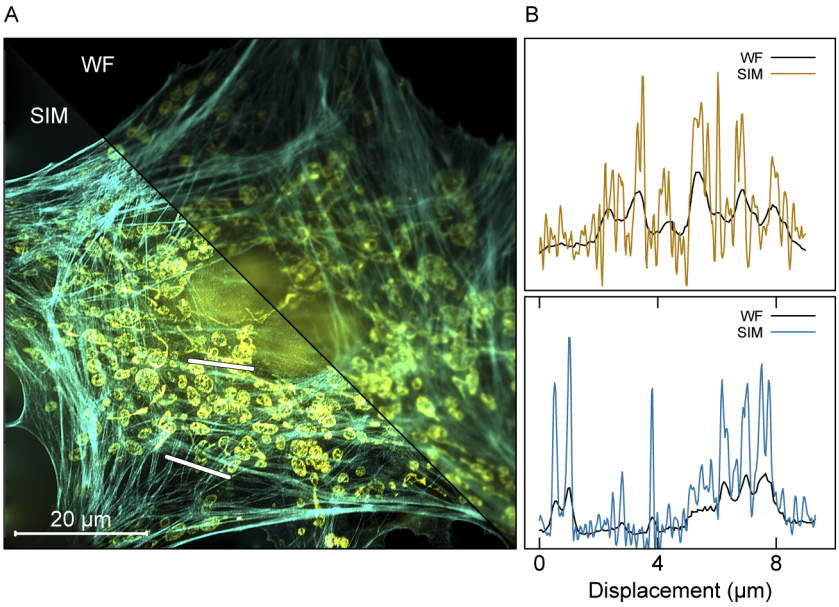

Fig. 6. Two-color imaging of BPAE cells. **A**. Widefield (upper right) and SIM (lower left) images of a BPAE cell showing actin filaments in the 473 nm channel (cyan), and mitochondria in the 532 nm channel (yellow). Images are displayed in ADU. **B**. One-dimensional cuts plotted along the lines illustrated in A. We show the widefield image (black line) and SR-SIM image (colored line) for the 473 nm excitation (bottom) corresponding to the lower line in A. and 532 nm excitation (top) corresponding to the upper line in A. The SIM traces show significant enhancement of resolution and features which cannot be distinguished in the widefield image.

of 50 ms for raw SIM images, corresponding to 0.45 s per color and 1.65 s for a full three-color image. We chose the longest acquisition time such that mitochondria and lysosome dynamics were negligible during the 9 SIM images, which maximizes the SIM SNR. A single frame is shown in Fig. 7, demonstrating enhanced contrast in the SIM image for the mitochondria and lysosomes and reveals branching of actin filaments which cannot be resolved in the widefield. Applying decorrelation analysis to the Wiener filtered widefield and SIM images, we find SIM leads to resolution enhancement of 1.3, 1.65, and 1.4 in the 465 nm, 532 nm, and 635 nm channels respectively. The blue channel has a significant amount of background from out-of-focus features. Specializing to the region shown in Fig. 7(B) where this is minimized, we find the resolution enhancement is somewhat higher, 1.37. The smaller resolution enhancement values reported here versus for the Argo-SIM slide and fixed cells is likely a reflection of the lower SNR achieved in this measurement.

Our setup can realize a raw frame rate of ~330 Hz, limited by the speed of our DAQ (TriggerScope 3B). Using a fast DAQ would allow us to reach the maximum exposure rate allowed by the DMD, 10 kHz, and replacing the DMD used here with the fastest available model could enable a 30 kHz frame rate. In most experiments, either sample properties, such as SNR and fluorophore brightness, or camera electronics impose significantly slower speed limits, but the high potential speed of DMD based setups could be advantageous in some situations. For example, ferroelectric SLM based Hessian TIRF-SIM experiments have reached exposure times as low as 0.5 ms for a ~17 µm×8 µm field of view, but slow SLM operation limited the raw frame rate to ~870 Hz [51].

Biomedical Optics EXPRESS

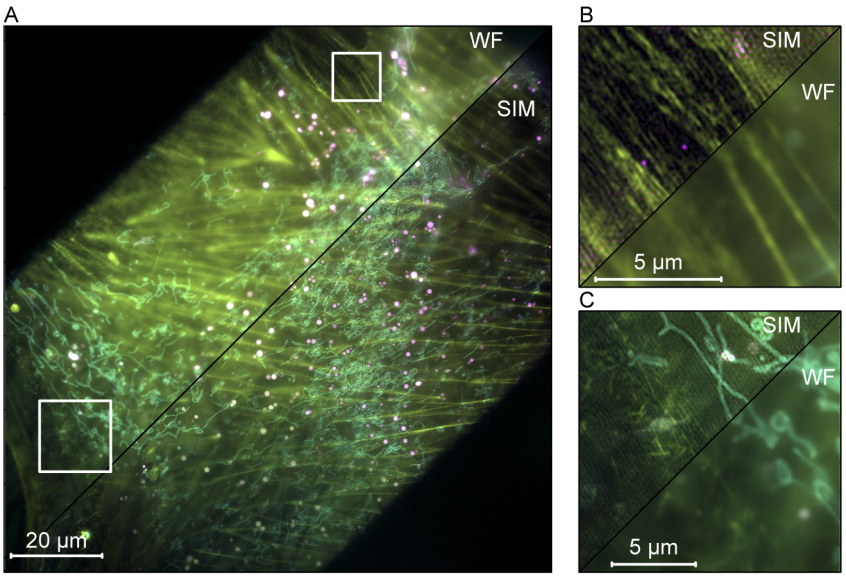

Fig. 7. Three-color imaging of live human adenocarcinoma epithelial cells. A. Widefield (upper left) and SIM (lower right) image of human adenocarcinoma epithelial cell actin filaments (yellow) in the 532 nm channel, lysosomes (magenta) in the 635 nm channel, and mitochondria (cyan) in the 465 nm channel. The field of view is limited by the size of the DMD, which is visible as the bright rectangular region in the image. Images are displayed in ADU. **B**. Widefield and SIM images of the upper-right region of interest illustrating resolution enhancement for several longer actin filaments. **C**. Widefield (lower right) and SIM (upper left) images of the lower region of interest illustrated in A. Resolution enhancement is visible for the mitochondria and actin filaments. Various short actin filaments that are difficult to see in the widefield image are visible in the SIM image with higher contrast, and their width is considerably narrowed.

4. Discussion and conclusions

Multi-wavelength coherent SIM is regularly achieved using diffraction gratings or LCoS SLM's for fringe projection, but the maximum achievable pattern display rate is limited by physical translation and rotation of the grating or the refresh rate of the SLM. Here, we provide a new theoretical framework to leverage a single DMD as a polychromatic diffractive optic for multi-wavelength coherent SIM, extending previous work [43,44]. Our work significantly differs from previous SIM approaches using multi-wavelength incoherent LED light sources or multi-wavelength incoherent image projection using a DMD [45,60]. In the current work, the maximum resolution is governed by the coherent transfer function and does not require hundreds to thousands of raw images to generate a SIM image, or require scanning.

This opens the possibility for quantitative, multi-wavelength pattern formation at rates up to 30 kHz for a factor of ~5 lower cost than LCoS SLM based units. While SIM imaging rates are ultimately limited by signal-to-noise ratio and phototoxicity, fast control of multi-wavelength pattern formation also provides new avenues in the design of multi-wavelength tomography [1,2], multi-wavelength optical trapping [3–5,7], high-speed tracking of photostable fluorescent labels below the diffraction limit [61], and high-speed modulation enhanced localization microscopy in multiple colors [37–41].

Future improvements to our approach may include extension to more wavelengths (see Supplemental Note 2 in Supplement 1), 3D-SIM [35,36], online GPU processing to speed

Biomedical Optics EXPRESS

reconstruction [34], specialized pattern generation to account for rolling shutters [62], and multiple cameras to speed multi-wavelength acquisition. Ease of alignment and instrument flexibility could be improved by removing the need for the Fourier mask. This could be achieved by developing a SIM reconstruction algorithm capable of accounting for the parasitic diffraction peaks, an approach that would require a detailed DMD forward model such as the one presented here. Implementing adaptive optics corrections could improve imaging quality and reduce artifacts, as has previously been reported [55,63].

Funding. National Heart, Lung, and Blood Institute (R01HL068702).

Acknowledgments. We thank Drs. Randy Bartels, Thomas Huser, Marcel Müller, and Andrew York for helpful discussions on the use of a DMD as an active diffractive element. Theoretical model, numerical simulations, hardware design and construction, software development, and instrument validation: PTB. Sample preparation and imaging: RK, GJS, PTB, DPS. Original concept, project management, and writing of manuscript: PTB, DPS.

Disclosures. The authors declare no conflicts of interest.

Data availability. Data underlying the results presented in this paper are available on Zenodo [64].

Supplemental document. See Supplement 1 for supporting content.

References

1. S. Chowdhury, W. J. Eldridge, A. Wax, and J. A. Izatt, "Structured illumination microscopy for dual-modality 3D sub-diffraction resolution fluorescence and refractive-index reconstruction," Biomed. Opt. Express **8**(12), 5776–5793 (2017).
2. S. Shin, D. Kim, K. Kim, and Y. Park, "Super-resolution three-dimensional fluorescence and optical diffraction tomography of live cells using structured illumination generated by a digital micromirror device," Sci. Rep. **8**(1), 9183 (2018).
3. F. M. Fazal and S. M. Block, "Optical tweezers study life under tension," Nat. Photonics **5**(6), 318–321 (2011).
4. M. J. Comstock, T. Ha, and Y. R. Chemla, "Ultrahigh-resolution optical trap with single-fluorophore sensitivity," Nat. Methods **8**(4), 335–340 (2011).
5. C. Muldoon, L. Brandt, J. Dong, D. Stuart, E. Brainis, M. Himsworth, and A. Kuhn, "Control and manipulation of cold atoms in optical tweezers," New J. Phys. **14**(7), 073051 (2012).
6. M. J. Booth, "Adaptive optics in microscopy," Philos. Trans. R. Soc., A **365**(1861), 2829–2843 (2007).
7. P. Zupancic, P. M. Preiss, R. Ma, A. Lukin, M. E. Tai, M. Rispoli, R. Islam, and M. Greiner, "Ultra-precise holographic beam shaping for microscopic quantum control," Opt. Express **24**(13), 13881 (2016).
8. P. T. Brown, D. Mitra, E. Guardado-Sanchez, R. Nourafkan, A. Reymbaut, C.-D. Hébert, S. Bergeron, A.-M. S. Tremblay, J. Kokalj, D. A. Huse, P. Schauß, and W. S. Bakr, "Bad metallic transport in a cold atom Fermi-Hubbard system," Science **363**(6425), 379–382 (2019).
9. G. Patterson, M. Davidson, S. Manley, and J. Lippincott-Schwartz, "Superresolution imaging using single-molecule localization," Annu. Rev. Phys. Chem. **61**(1), 345–367 (2010).
10. J. Alvelid and I. Testa, "Fluorescence microscopy at the molecular scale," Curr. Opin. Biomed. Eng. **12**, 34–42 (2019).
11. T. Dertinger, R. Colyer, G. Iyer, S. Weiss, and J. Enderlein, "Fast, background-free, 3D super-resolution optical fluctuation imaging (SOFI)," Proc. Natl. Acad. Sci. U. S. A. **106**(52), 22287–22292 (2009).
12. S. Culley, K. L. Tosheva, P. Matos Pereira, and R. Henriques, "SRRF: Universal live-cell super-resolution microscopy," Int. J. Biochem. Cell Biol. **101**, 74–79 (2018).
13. S. W. Hell and J. Wichmann, "Breaking the diffraction resolution limit by stimulated emission: stimulated-emission-depletion fluorescence microscopy," Opt. Lett. **19**(11), 780 (1994).
14. T. A. Klar, S. Jakobs, M. Dyba, A. Egner, and S. W. Hell, "Fluorescence microscopy with diffraction resolution barrier broken by stimulated emission," Proc. Natl. Acad. Sci. **97**(15), 8206–8210 (2000).
15. K. C. Gwosch, J. K. Pape, F. Balzarotti, P. Hoess, J. Ellenberg, J. Ries, and S. W. Hell, "MINFLUX nanoscopy delivers 3D multicolor nanometer resolution in cells," Nat. Methods **17**(2), 217–224 (2020).
16. M. Weber, M. Leutenegger, S. Stoldt, S. Jakobs, T. S. Mihaila, A. N. Butkevich, and S. W. Hell, "MINSTED fluorescence localization and nanoscopy," Nat. Photonics **15**(5), 361–366 (2021).
17. M. Hofmann, C. Eggeling, S. Jakobs, and S. W. Hell, "Breaking the diffraction barrier in fluorescence microscopy at low light intensities by using reversibly photoswitchable proteins," Proc. Natl. Acad. Sci. **102**(49), 17565–17569 (2005).
18. L. A. Masullo, A. Bodén, F. Pennacchietti, G. Coceano, M. Ratz, and I. Testa, "Enhanced photon collection enables four dimensional fluorescence nanoscopy of living systems," Nat. Commun. **9**(1), 3281 (2018).
19. R. Heintzmann and C. G. Cremer, "Laterally modulated excitation microscopy: improvement of resolution by using a diffraction grating," in *Optical Biopsies and Microscopic Techniques III*, I. J. Bigio, H. Schneckenburger, J. Slavik, K. Svanberg, and P. M. Viallet, eds. (SPIE, 1999).

Biomedical Optics EXPRESS

20. M. G. L. Gustafsson, "Surpassing the lateral resolution limit by a factor of two using structured illumination microscopy," J. Microsc. **198**(2), 82–87 (2000).
21. B. Bailey, D. L. Farkas, D. L. Taylor, and F. Lanni, "Enhancement of axial resolution in fluorescence microscopy by standing-wave excitation," Nature **366**(6450), 44–48 (1993).
22. M. A. A. Neil, R. Juškaitis, and T. Wilson, "Method of obtaining optical sectioning by using structured light in a conventional microscope," Opt. Lett. **22**(24), 1905 (1997).
23. M. G. L. Gustafsson, D. A. Agard, and J. W. Sedat, "Doubling the lateral resolution of wide-field fluorescence microscopy using structured illumination," in *Three-Dimensional and Multidimensional Microscopy: Image Acquisition Processing VII*, J.-A. Conchello, C. J. Cogswell, A. G. Tescher, and T. Wilson, eds. (SPIE, 2000).
24. J. T. Frohn, H. F. Knapp, and A. Stemmer, "True optical resolution beyond the Rayleigh limit achieved by standing wave illumination," Proc. Natl. Acad. Sci. **97**(13), 7232–7236 (2000).
25. J. T. Frohn, H. F. Knapp, and A. Stemmer, "Three-dimensional resolution enhancement in fluorescence microscopy by harmonic excitation," Opt. Lett. **26**(11), 828 (2001).
26. M. G. Gustafsson, L. Shao, P. M. Carlton, C. J. R. Wang, I. N. Golubovskaya, W. Z. Cande, D. A. Agard, and J. W. Sedat, "Three-dimensional resolution doubling in wide-field fluorescence microscopy by structured illumination," Biophys. J. **94**(12), 4957–4970 (2008).
27. L. Schermelleh, P. M. Carlton, S. Haase, L. Shao, L. Winoto, P. Kner, B. Burke, M. C. Cardoso, D. A. Agard, M. G. L. Gustafsson, H. Leonhardt, and J. W. Sedat, "Subdiffraction multicolor imaging of the nuclear periphery with 3D structured illumination microscopy," Science **320**(5881), 1332–1336 (2008).
28. J. D. Manton, F. Ströhl, R. Fiolka, C. F. Kaminski, and E. J. Rees, "Concepts for structured illumination microscopy with extended axial resolution through mirrored illumination," Biomed. Opt. Express **11**(4), 2098 (2020).
29. P. Kner, B. B. Chhun, E. R. Griffis, L. Winoto, and M. G. L. Gustafsson, "Super-resolution video microscopy of live cells by structured illumination," Nat. Methods **6**(5), 339–342 (2009).
30. L. M. Hirvonen, K. Wicker, O. Mandula, and R. Heintzmann, "Structured illumination microscopy of a living cell," Eur. Biophys. J. **38**(6), 807–812 (2009).
31. R. Förster, H.-W. Lu-Walther, A. Jost, M. Kielhorn, K. Wicker, and R. Heintzmann, "Simple structured illumination microscope setup with high acquisition speed by using a spatial light modulator," Opt. Express **22**(17), 20663 (2014).
32. H.-W. Lu-Walther, M. Kielhorn, R. Förster, A. Jost, K. Wicker, and R. Heintzmann, "fastSIM: a practical implementation of fast structured illumination microscopy," Methods Appl. Fluoresc. **3**(1), 014001 (2015).
33. M. Shaw, L. Zajiczek, and K. O'Holleran, "High speed structured illumination microscopy in optically thick samples," Methods **88**, 11–19 (2015).
34. A. Markwirth, M. Lachetta, V. Mönkemöller, R. Heintzmann, W. Hübner, T. Huser, and M. Müller, "Video-rate multi-color structured illumination microscopy with simultaneous real-time reconstruction," Nat. Commun. **10**(1), 4315 (2019).
35. L. Shao, P. Kner, E. H. Rego, and M. G. L. Gustafsson, "Super-resolution 3D microscopy of live whole cells using structured illumination," Nat. Methods **8**(12), 1044–1046 (2011).
36. R. Fiolka, L. Shao, E. H. Rego, M. W. Davidson, and M. G. L. Gustafsson, "Time-lapse two-color 3D imaging of live cells with doubled resolution using structured illumination," Proc. Natl. Acad. Sci. **109**(14), 5311–5315 (2012).
37. L. Reymond, J. Ziegler, C. Knapp, F.-C. Wang, T. Huser, V. Ruprecht, and S. Wieser, "SIMPLE: Structured illumination based point localization estimator with enhanced precision," Opt. Express **27**(17), 24578 (2019).
38. L. Reymond, T. Huser, V. Ruprecht, and S. Wieser, "Modulation-enhanced localization microscopy (meLM)," JPhys Photonics **2**(4), 041001 (2020).
39. P. Jouchet, C. Cabriel, N. Bourg, M. Bardou, C. Poüs, E. Fort, and S. Lévêque-Fort, "Nanometric axial localization of single fluorescent molecules with modulated excitation," Nat. Photonics **15**(4), 297–304 (2021).
40. J. Cnossen, T. Hinsdale, R. Ø. Thorsen, M. Siemons, F. Schueder, R. Jungmann, C. S. Smith, B. Rieger, and S. Stallinga, "Localization microscopy at doubled precision with patterned illumination," Nat. Methods **17**(1), 59–63 (2020).
41. L. Gu, Y. Li, S. Zhang, Y. Xue, W. Li, D. Li, T. Xu, and W. Ji, "Molecular resolution imaging by repetitive optical selective exposure," Nat. Methods **16**(11), 1114–1118 (2019).
42. L. J. Young, F. Ströhl, and C. F. Kaminski, "A guide to structured illumination TIRF microscopy at high speed with multiple colors," *J. Visualized Exp.* (111), 53988 (2016).
43. A. Sandmeyer, M. Lachetta, H. Sandmeyer, W. Hübner, T. Huser, and M. Müller, "DMD-based super-resolution structured illumination microscopy visualizes live cell dynamics at high speed and low cost," (2019). BioRxiv 10.1101/797670.
44. M. Li, Y. Li, W. Liu, A. Lal, S. Jiang, D. Jin, H. Yang, S. Wang, K. Zhanghao, and P. Xi, "Structured illumination microscopy using digital micro-mirror device and coherent light source," Appl. Phys. Lett. **116**(23), 233702 (2020).
45. D. Dan, M. Lei, B. Yao, W. Wang, M. Winterhalder, A. Zumbusch, Y. Qi, L. Xia, S. Yan, Y. Yang, P. Gao, T. Ye, and W. Zhao, "DMD-based LED-illumination super-resolution and optical sectioning microscopy," Sci. Rep. **3**(1), 1116 (2013).
46. K. Wicker and R. Heintzmann, "Resolving a misconception about structured illumination," Nat. Photonics **8**(5), 342–344 (2014).
47. Instruments Texas, "Using lasers with DLP DMD technology," TI DN **2509927** (2008).

Biomedical Optics EXPRESS

48. J. Liang, "High-precision laser beam shaping and image projection," Ph.D. thesis, The University of Texas at Austin (2012).
49. R. Casini and P. G. Nelson, "On the intensity distribution function of blazed reflective diffraction gratings," J. Opt. Soc. Am. A **31**(10), 2179 (2014).
50. N. W. Ashcroft and N. D. Mermin, *Solid State Physics* (Cengage Learning, Inc, 1976), chap. 5. The Reciprocal Lattice, pp. 85–94.
51. X. Huang, J. Fan, L. Li, H. Liu, R. Wu, Y. Wu, L. Wei, H. Mao, A. Lal, P. Xi, L. Tang, Y. Zhang, Y. Liu, S. Tan, and L. Chen, "Fast, long-term, super-resolution imaging with Hessian structured illumination microscopy," Nat. Biotechnol. **36**(5), 451–459 (2018).
52. A. Lal, C. Shan, and P. Xi, "Structured illumination microscopy image reconstruction algorithm," IEEE J. Sel. Top. Quantum Electron. **22**(4), 50–63 (2016).
53. P. T. Brown and D. P. Shepherd, "Qi2lab/mcsim," Zenodo (2021), Https://github.com/QI2lab/mcSIM.
54. B. M. Hanser, M. G. L. Gustafsson, D. A. Agard, and J. W. Sedat, "Phase retrieval for high-numerical-aperture optical systems," Opt. Lett. **28**(10), 801 (2003).
55. M. Žurauskas, I. M. Dobbie, R. M. Parton, M. A. Phillips, A. Göhler, I. Davis, and M. J. Booth, "IsoSense: frequency enhanced sensorless adaptive optics through structured illumination," Optica **6**(3), 370 (2019).
56. A. Descloux, K. S. Grußmayer, and A. Radenovic, "Parameter-free image resolution estimation based on decorrelation analysis," Nat. Methods **16**(9), 918–924 (2019).
57. J. Frank and M. van Heel, "Correspondence analysis of aligned images of biological particles," J. Mol. Biol. **161**(1), 134–137 (1982).
58. W. O. Saxton and W. Baumeister, "The correlation averaging of a regularly arranged bacterial cell envelope protein," J. Microsc. **127**(2), 127–138 (1982).
59. R. Van den Eynde, A. Sandmeyer, W. Vandenberg, S. Duwé, W. Hübner, T. Huser, P. Dedecker, and M. Müller, "Quantitative comparison of camera technologies for cost-effective super-resolution optical fluctuation imaging (SOFI)," JPhys Photonics **1**(4), 044001 (2019).
60. A. G. York, S. H. Parekh, D. D. Nogare, R. S. Fischer, K. Temprine, M. Mione, A. B. Chitnis, C. A. Combs, and H. Shroff, "Resolution doubling in live, multicellular organisms via multifocal structured illumination microscopy," Nat. Methods **9**(7), 749–754 (2012).
61. K. Drescher, J. Dunkel, L. H. Cisneros, S. Ganguly, and R. E. Goldstein, "Fluid dynamics and noise in bacterial cell-cell and cell-surface scattering," Proc. Natl. Acad. Sci. U. S. A. **108**(27), 10940–10945 (2011).
62. L. Song, H.-W. Lu-Walther, R. Förster, A. Jost, M. Kielhorn, J. Zhou, and R. Heintzmann, "Fast structured illumination microscopy using rolling shutter cameras," Meas. Sci. Technol. **27**(5), 055401 (2016).
63. R. Turcotte, Y. Liang, M. Tanimoto, Q. Zhang, Z. Li, M. Koyama, E. Betzig, and N. Ji, "Dynamic super-resolution structured illumination imaging in the living brain," Proc. Natl. Acad. Sci. **116**(19), 9586–9591 (2019).
64. P. T. Brown and D. P. Shepherd, "Data associated with Multicolor structured illumination microscopy and quantitative control of polychromatic coherent light with a digital micromirror device," figshare (2020) [retrieved 21 February 2020], https://doi.org/10.5281/zenodo.4313345.